Femtosecond-laser direct-write photoconductive patterns on tellurite glass

Gözden Torun,[1,*] Anastasia Romashkina,[1] Tetsuo Kishi,[2] and Yves Bellouard[1]

[1] *Galatea Laboratory, STI/IEM, Ecole Polytechnique Fédérale de Lausanne (EPFL), 2002 Neuchâtel, Switzerland*

[2] *Department of Materials Science and Engineering, Tokyo Institute of Technology, 152-8552, Tokyo, Japan*

(Received 20 April 2023; revised 22 September 2023; accepted 17 November 2023; published 5 January 2024)

We report the formation of arbitrary photoconductive patterns made of tellurium (Te) nanocrystals by exposing a tellurite (TeO_2-based) glass to femtosecond laser pulses. During this process, Te/TeO_2-glass nanocomposite interfaces with photoconductive properties form on the tellurite glass substrate. We show that these laser-written patterns exhibit a photoresponse, from the near ultraviolet (263 nm) to the visible spectrum, stable over a few months. Specifically, high responsivity (16.55 A/W) and detectivity (5.25×10^{11} Jones) of a single laser-written line pattern are measured for an illumination dose of 0.07 mW/cm^2 at 400 nm. This work illustrates a pathway for locally turning a tellurite glass into a functional photoconductor of arbitrary shape, without adding materials and using a single laser process step.

DOI: 10.1103/PhysRevApplied.21.014008

I. INTRODUCTION

Recently, we demonstrated that upon near-IR femtosecond (fs) laser exposure, the tellurite (TeO_2-based) glass evolves into a semiconductor-glass composite [1] consisting of trigonal tellurium (*t*-Te) nanocrystals embedded in a TeO_2 glass matrix. Extensive investigation revealed that the laser-modified zones show evidence of *t*-Te nanoparticles and nanocrystals with a low amount of amorphous Te(*a*-Te) upon a single femtosecond laser pulse exposure of TeO_2-based glass [2]. In particular, it leads to the formation of a Te/TeO_2-glass interface at the surface, at which the ratio of phases depends on the laser-processing parameters. This process is based on a scalable laser direct-write technology by focusing a femtosecond laser on the surface of a glass substrate and scanning the laser spot to form patterns with arbitrary lengths and shapes.

Several authors reported the production of TeO_2/Te interface by surface oxidation of pure tellurium thin films [3–6]. In these studies, the oxidation process was driven by ultraviolet (UV) irradiation or by cw lasers operating at 440–520 nm [7], and several functional properties, e.g., photoconductivity [3,4,8,9], ultrahigh chemical sensitivity [10,11], and better optical properties than Te and TeO_2 [12], were demonstrated. Here, we follow a different path. Starting from glass, a TeO_2-based transparent substrate of arbitrary thickness, we use femtosecond laser pulses to *transform* it into a pure *t*-Te phase locally and with micron-scale resolution. Apart from its inherent versatility since any patterns can be produced on any substrate form and size in an open air at room temperature, this approach has the potential to be simple, efficient, and economical. Thanks to a single process, *the functional device is produced by transforming a plain glass substrate locally without adding any other materials*.

In the following, we demonstrate this concept by investigating the photoconductive properties of the Te/TeO_2-glass interface produced by direct-write femtosecond laser exposure. Specifically, we unravel a highly reproducible photoresponse under different illumination conditions in the near ultraviolet to the visible (UV-VIS) spectrum that we characterize for various laser-exposure parameters and illumination conditions. This single process is particularly appealing for light-sensing devices of arbitrary sizes and shapes made by functionalizing a single piece of material.

II. EXPERIMENTAL SECTION AND METHODS

A. Glass-substrate preparation and femtosecond-laser micromachining

The glass composition tested in this study is $10K_2O$-$10WO_3$-$80TeO_2$ (mol%). Commercial powders were mixed and melted in an Au crucible at around 973 K for 30 min in an electric furnace to produce the substrates. The

*gozden.torun@epfl.ch

Published by the American Physical Society under the terms of the Creative Commons Attribution 4.0 International license. Further distribution of this work must maintain attribution to the author(s) and the published article's title, journal citation, and DOI.

melt was then quenched onto a brass plate. After quenching, the sample was crushed and remelted at 973 K for 30 min, followed by subsequent annealing at 598 K for 1 h. The so-obtained glass rods were cut and optically polished to samples with a thickness of 1 mm for further optical characterization and femtosecond-laser machining.

A Yb-doped femtosecond fiber laser (Yuzu from Amplitude) emitting 270-fs pulses at 1030 nm was used in this experiment. Laser patterns consisting of parallel lines with several lengths from 1 to 10 mm were inscribed on the surface of the tellurite glass. The specimen was translated under the laser focus using high-precision motorized stages (Ultra-HR from PI Micos). The laser beam was focused on the surface of the sample using a 0.4 numerical aperture (NA) objective (OFR-20×-1064 nm from Thorlabs), resulting in a spot size (defined at $1/e^2$) of approximately 1.97 μm. The repetition rate was fixed at 1 MHz, corresponding to a thermal cumulative regime for tellurite glass [1]. Here, the number of effective pulses per spot varies from 20 to 4000, and the range of pulse energy spans from 1 to 200 nJ, resulting in an incoming net fluence ranging from 0.0066 to 263 J/mm^2. Further details on the exposure parameters can be found in our previous study [2].

B. Sample characterization

After laser exposure, the tellurite glass samples were first observed using an optical microscope (OM, BX51 from Olympus). A Raman spectrometer (LabRam HR from Horiba), equipped with a 532-nm laser excitation source attenuated down to 4 mW, focused with a 0.9 NA objective (100×-532 nm from Thorlabs) down to a micron-size spot was then used to confirm the presence of elemental Te nanocrystals in laser-modified zones. Further, another Raman spectrometer (MonoVista CRS+ from Spectroscopy & Imaging GmbH), equipped with a 442-nm laser-excitation source (He-Cd laser from Kimmon Koha) with an incident power of 115 mW was used to investigate the degradation mechanism under UV-light irradiation. The linearly polarized Raman laser beam was focused on the surface of the glass sample using a 0.9 NA objective (50×-532 nm from Thorlabs). A series of point scans were performed with acquisition times of 60 s per individual spot. Finally, the absorption spectra were measured at room temperature for wavelengths ranging from 250 to 2500 nm using an ultraviolet-visible-near-infrared spectrometer (UV-VIS-NIR, Lambda 950 from Perkin Elmer). For this purpose and to isolate the functionalized regions in the substrate, a mask with a hole of around 2×2 mm^2 was cut out of a paper sheet for broadband absorbance. For the measurement, the reference beam power was attenuated to 10% to compensate for the presence of the mask and to ensure the effective reduction of the beam size from the original 2 cm in diameter. The thickness of the sample used for this transmission measurement was 2 mm.

C. Electrical measurement, device fabrication, and characterization

First, the dc resistivity of the laser-written tracks was measured by a four-probe station equipped with a microscope connected to a source measurement unit (SMU B2902A from Keysight) applying a bias voltage of 40 V. A control software (Quick I/V Measurement Software from Keysight) was used to obtain the data. The tungsten probes were placed on the sample with the help of high-precision adjustments. The conductivity temperature dependence was measured by slowly heating the sample from room temperature to 368 K using a heating stage.

To fabricate the device used for probing the photoconductivity, thin gold electrodes (approximately 20 nm thick) were sputtered (JFC-1200 Fine Coater from JEOL). For obtaining the desired shape of electrodes, a hard mask made from fused silica glass by a femtosecond-laser machining-assisted etching process was directly placed on the tellurite glass before sputtering, as shown in Fig. S1 (see Supplemental Material [13]). Later, wire bonding (HB10 wedge and ball bonder from TPT) with either Au or Al wires was used to interface the glass laser-written lines with a standard printed circuit board (PCB). To ensure the wires were attached to the sample and the PCB over long measurement periods, the electrodes were covered with Ag-based electrically conductive epoxy (H20E-FC from epoxy technology; the resistivity is less than 0.04 Ω m at room temperature). The epoxy was later cured at 393 K for 15 min.

After the device fabrication, characteristic transient current-voltage responses were collected with a source measurement unit (SMU B2902A from Keysight). Various light sources were used for the photoconductivity measurements: a white-light LED (spectral range spanning from 450 to 750 nm) and three other LEDs with central wavelengths at 460, 400, and 263 nm emitting various optical intensities (up to 2.1 mW/cm^2). The spectral profiles of the LED sources are presented in Fig. S2 (see Supplemental Material [13]). After collimation, a cylindrical lens was used to create a stretched elliptical illumination profile covering the laser-written patterns with an area of approximately 200 mm^2. The same measurement was performed for at least ten different lines for statistical purposes and over a few months to investigate the long-term stability of the material transformation. Here, 1 month refers to 30 days of consecutive measurements. Figure 1 illustrates a schematic representation of the device fabrication and the characterization procedure.

III. RESULTS AND DISCUSSION

A. Electrical and optical properties

The electrical conductivity of pure TeO_2 glass and binary TeO_2 glass systems are based on a small radius

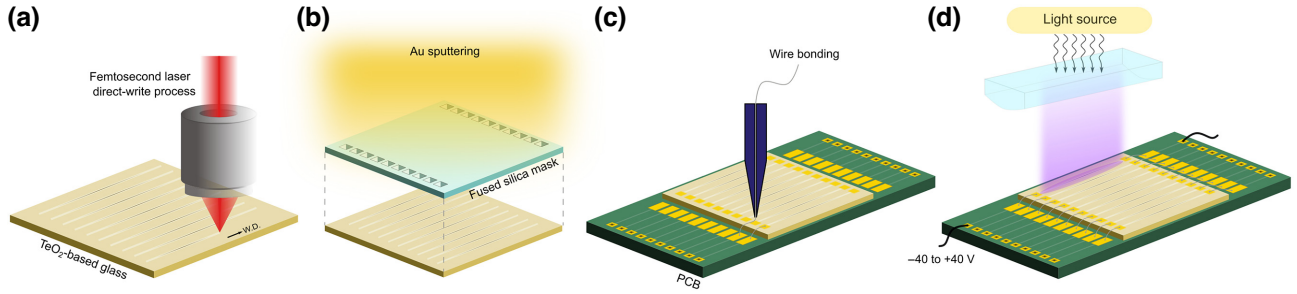

FIG. 1. Schematic representations of the device preparation steps (a)–(c) and photoconductivity characterization method (d). (a) Femtosecond-laser direct-write process applied to tellurite glass: the line patterns were produced by moving the specimen under the laser beam at a prescribed velocity. (b) The fabrication of Au electrodes at both ends of the sample was performed by sputtering the metal through a hard mask to protect the central portion. (c) Wire bonding was used to connect the electrodes on the specimen to a standard PCB on which the glass substrate was mounted. (d) Device characterization was performed by applying a bias voltage ranging from −40 to +40 V through the PCB pins. The illumination source for photoconductivity characterization was delivered in the form of a thin elliptical spot exposing individual line patterns separately.

polaron hopping mechanism at and above room temperature [14]. Depending on the glass modifier oxides, there can be an additional contribution from ionic conductivity. The composition studied in this work [$10K_2O$-$10WO_3$-$80TeO_2$ (mol%)] has a reported electrical resistivity (dc) at room temperature of 1.4×10^{18} Ω m (drops to 1.14×10^{14} Ω m at 373 K) [15].

Figure 2 illustrates electrical properties, such as the effect of laser-processing parameters and temperature on the resistivity of the Te/TeO_2-glass nanocomposite interface, and optical properties, such as absorption spectra, direct and indirect band-gap plots for the pristine and laser-modified area. The resistivity of the pattern was calculated from the measured resistance and its effective dimensions [i.e., cross section and length derived from both the images taken by OM and transmission electron microscopy (TEM) [2], respectively]. The resistivity of the pattern decays from approximately 50 Ω m to approximately 0.001 Ω m with the increasing number of pulses [Fig. 2(a)]. Several parameters, such as the surface area of grain boundaries, preferred grain orientation, presence of impurities, crystallographic defects (vacancies), and other structural defects, influence dc resistivity [16]. We showed that the laser-modified area consists of Te nanocrystals (with a grain size range of approximately 5–15 nm) growing proportionally with the number of laser pulses and the laser electric field intensity [2]. Low laser fluence results in thinner crystallized areas with disconnected nanocrystals, more susceptible to charges, impurities at the interface, and surface scattering. Through the grain-growth mechanism stimulated by higher laser fluence in the thermal-cumulative regime, the value reaches the resistivity of polycrystalline bulk Te [17–19]. However, no correlation was observed between the orientation of the laser electric field and the resistivity of line patterns. All patterns tested from this point were written at a pulse energy of 200 nJ and with 4000 pulses per focal spot (corresponding to an incoming pulse fluence of 262 J/mm^2).

Figure 2(b) shows the temperature-dependent relative resistivity of the laser-written lines, reflecting a typical semiconductor behavior due to the thermally active charge transportation. The inset illustrates the activation energy, estimated to be approximately 0.6 meV using an Arrhenius-law fitting procedure (ln R_T vs. 10^3/T) [16,20,21].

Figure 2(c) presents the absorption spectra of the *pristine glass* versus the *laser-written area* of 2×2 mm^2. The laser-written area shows broadband absorption in the solar spectral emission range, decreasing continuously towards the bandgap energy of *t*-Te (0.34 eV or 3600 nm). While it is above 80% in the visible spectrum, there is a sharp rise in absorption below 460 nm, reaching the maximum value between 330–410 nm. It was reported elsewhere that Te nanoparticles between 10 and 120 nm show a plasmoniclike resonance-dominated transition in the spectral range approximately 300 to 400 nm [22]. There, similar to our study in which the size of nanocrystals and nanoparticles is distributed between approximately 5 and 55 nm, the absorption spectra of Te nanoparticles (with sizes ranging from 10 to 300 nm) cover the entire solar-emission spectrum from 300 to 2000 nm [22]. The absorption spectra can be modulated by the laser-writing parameters, as shown in Fig. S3 (see Supplemental Material [13]).

Figure 2(d) shows Tauc plots [23] of both direct and indirect band-gap model behaviors. While a linear region (and hence, a band-gap value) is identifiable for the nonexposed case, the laser-exposed regions exhibit less pronounced linear zones that may account for their disorganized structures and interfacial effects. A shift towards lower energy, both in the direct and indirect optical band-gap models, is observed as an expected consequence of the presence of Te nanocrystals after laser exposure.

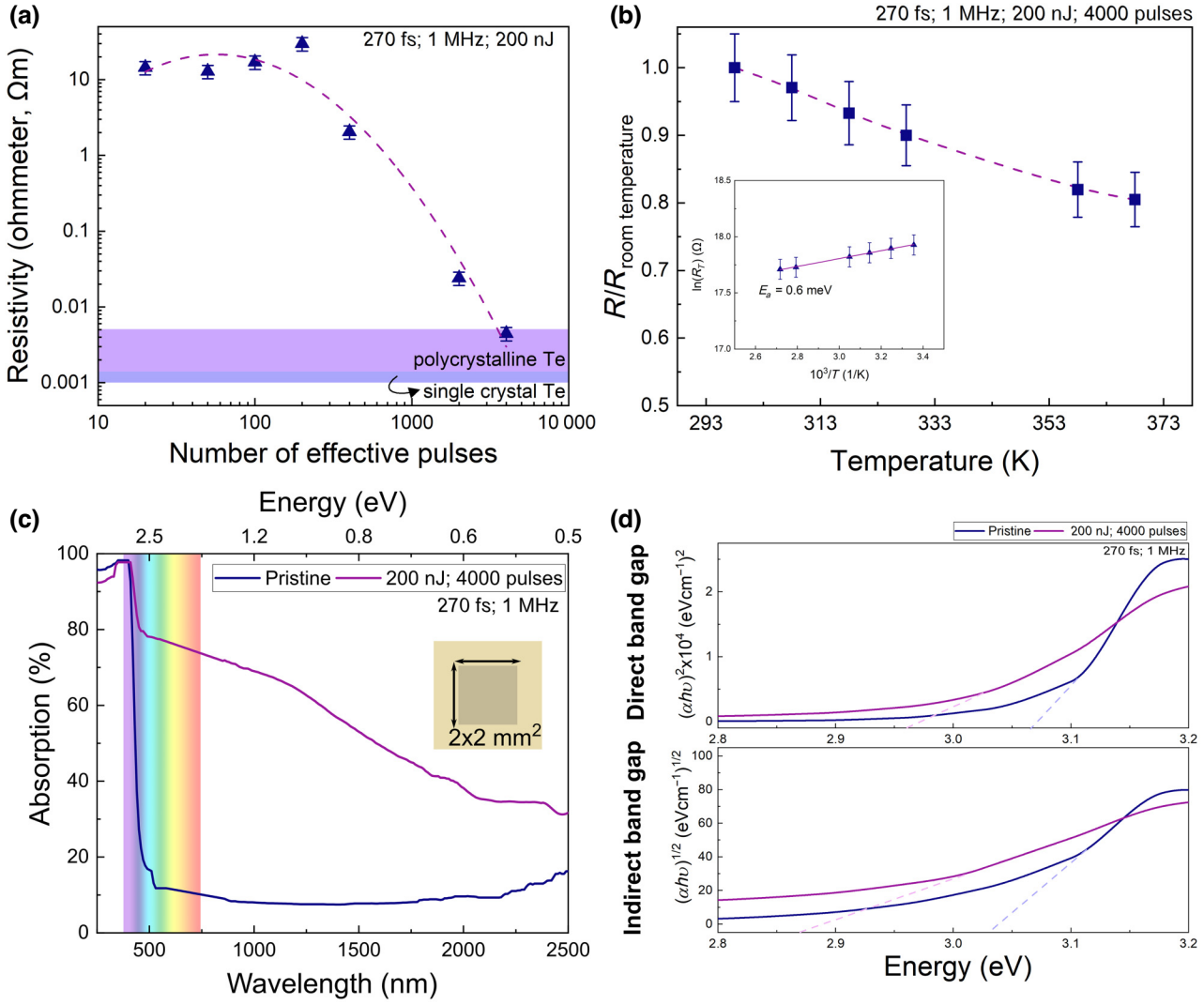

FIG. 2. (a) Effect of the laser-writing parameters on electrical (dc) resistivity of line patterns. (b) Effect of the temperature on the resistivity of laser-written patterns with the inset image of the Arrhenius-law fitting. (c) Measured UV-VIS-NIR absorption spectra of the pristine and laser-written area (2×2 mm^2). (d) Corresponding Tauc plots of pristine and the laser-written area, considering both indirect and direct band-gap absorption models.

B. Photoconductive properties and long-term stability

The p-type behavior of Te originates from the p-state lone-pair electrons that form the upper level of the valence band [24]. The population of holes in the p-type conduction band comes from the interaction of these lone-pair electrons with dangling bonds. The photoconductivity can occur at interfaces, such as at the surface or within grain boundaries, due to vacancies or impurities, due to the variation in hole concentration [11]. In the present case, the laser-modified zone consists of a heterogeneous structure of polycrystalline Te, amorphous Te, and TeO_2 in a glassy phase [2]. The photoconductivity involves multiple conduction mechanisms as opposed to simpler, well-defined Te/TeO_2 interfaces as reported in Refs. [3,4,8]. In addition, gas surface adsorption processes, affecting the population of holes can take place during the measurement [4,5,11].

To avoid manual manipulations while testing the photoconductivity of the laser-written patterns, we designed a specific device in coplanar configuration, illustrated in Fig. 1(d). The electrodes in the form of a thin film of Au at both ends of the line patterns are connected to a PCB by wire bonding. We conducted a current-voltage (I-V) characterization and calculated their responsivity, detectivity, external quantum efficiency, and generated photocurrent by varying optical power density. Additionally, we determined the spectral and temporal photoresponses of the patterns. The results are gathered in Fig. 3.

The spectral response of the Te/TeO_2-glass nanocomposite is demonstrated in Fig. 3(a). It exhibits a strong

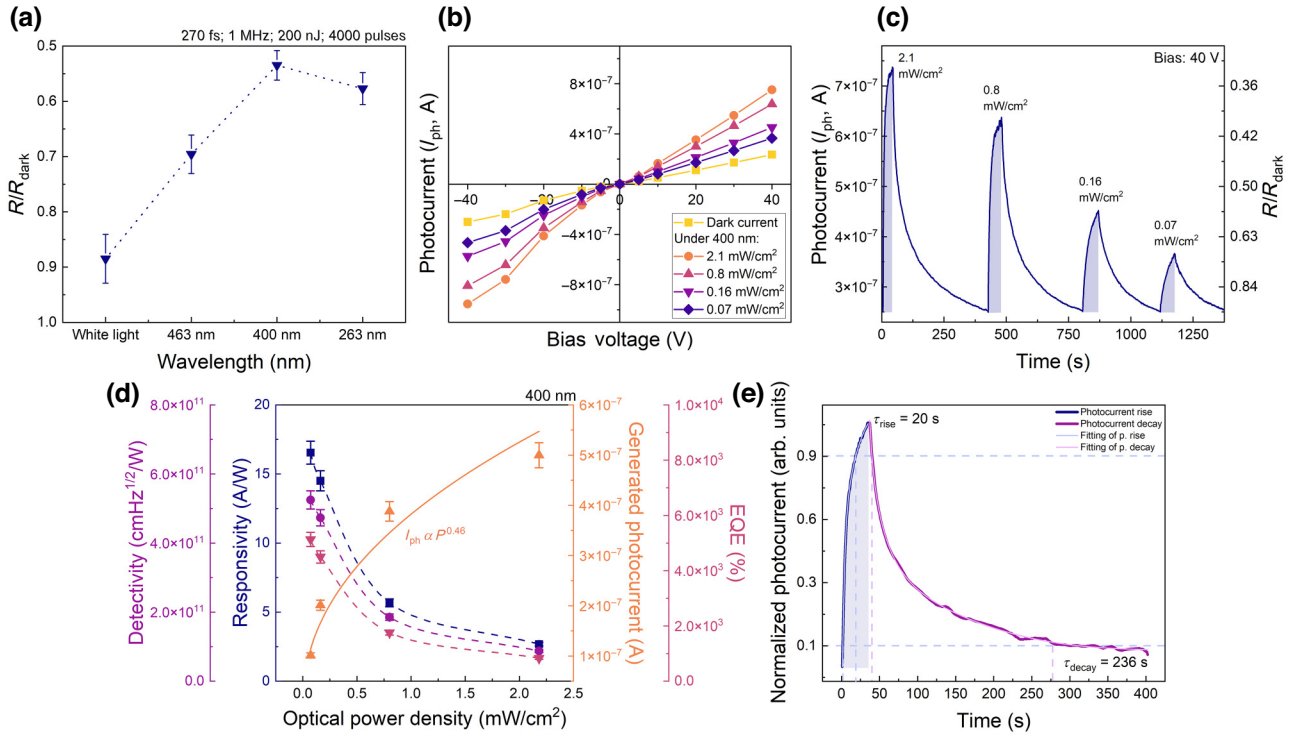

FIG. 3. (a) Spectral response of the device per unit of incident light power. (b) *I-V* curve with and without illumination with various voltage biases (−40 V to +40 V). (c) Typical temporal evolution with different optical power densities (0.07–2.1 mW/cm^2). (e) Responsivity, detectivity, EQE (%), and generated photocurrent of Te/TeO_2-glass nanocomposite structure. (e) Photocurrent rise and decay time for a line pattern. All measurements are performed under an open-air atmosphere at room temperature.

absorption at approximately 400 nm, leading to the highest photocurrent output. The spectrum of the white light is presented in Fig. S2 (see Supplemental Material [13]). Although the center peak is located at approximately 600 nm, radiation below 460 nm can contribute to the observed photoresponse under white-light illumination. *I-V* curves obtained without and with illumination in both forward and reverse bias are displayed in Fig. 3(b). The typical *I-V* curve deviates from Ohmic contact in the range of −40 V to +40 V. The absolute semilog *I-V* curve is presented in Fig. S4 (see Supplemental Material [13]). In the dark current for a zero-bias voltage, we measure near-zero current ($3.7 \times 10^{-10} \pm 1 \times 10^{-10}$ A). The electrical conductivity in the device is controlled mainly by the conductive part of the laser-modified zones, interfaces, and structural impurities and defects [25]. For the current to flow, the device in this scheme requires a bias voltage above zero. Once the bias voltage exceeds the internal barrier voltage (around 1 V in this case) and the knee voltage (or breakdown voltage for reverse bias) is surpassed, the external electric field supplies extra carriers. By illuminating the active area of the device, the current rises as a function of optical power density. The photocurrent at 400 nm versus optical power density follows a typical square-root-like relation, typically observed in the case of high resistances.

Figure 3(c) shows the temporal response of laser-written patterns under the illumination of 400 nm with different optical power densities. From this graph, we calculated the responsivity (R_{ph}), detectivity (D^*), and external quantum efficiency (EQE), which are a figure of merit (FOM) for the photodetecting properties of our laser-written patterns on tellurite glass. R indicates the generated photocurrent per unit area, D^* displays the ability to differentiate weak signals from noise, and EQE the number of charge carriers (electron-hole pairs) collected per photon incident on the photodetector [26]. They are expressed as

$$R_{ph} = \frac{\Delta I}{AP}, \text{where } \Delta I = I_{ph} = I_{light} - I_{dark},$$

$$D^* = \frac{R_{ph}\sqrt{A}}{\sqrt{2eI_{dark}}},$$

$$\text{EQE } (\%) = \left(\frac{hcR_{ph}}{e\lambda}\right) \approx \left[\frac{R_{ph}}{\lambda}\right] \times 1240 \left(W\frac{nm}{A}\right),$$

where I_{ph}, I_{light}, I_{dark}, P, A, e, h, c, λ are the generated photocurrent, the current measured under illumination, the dark current, optical power density, the effective covered area with Te on the TeO_2-based glass, the charge of an electron, the Planck constant, the speed of light, and the

illumination source wavelength, respectively. At 400 nm and under an exposure dose of 0.07 mW/cm^2, the peak responsivity and detectivity of the device are calculated to be approximately 16.55 A/W and 5.25×10^{11} Jones, respectively. The responsivity is reduced with the optical power density, a behavior similar to various Te photodetectors [4,8,27–30], which is attributed to defect states in the laser-modified zones. Photogenerated holes under low optical intensity are captured by the defect states near the valence band and reduce the amount of recombination of electron-hole pairs. However, under high optical intensity, a low number of photogenerated holes are captured, due to the limited number of defect states. Therefore, the laser-modified zone is more sensitive under lower light intensities. A similar trend is observed in the EQE (%) plot, which is directly proportional to the responsivity and inversely proportional to the light intensity. Note that the calculated responsivity, detectivity, and EQE indicate the peak values, which can alternate due to geometrical uncertainties, i.e., fluctuation in the active part of the laser-modified width, connectivity, and homogeneity of nanocrystals in the laser-modified zone. The generated photocurrent follows an empiric power law in the form:

$$I_{\text{ph}} = \beta P^{\alpha},$$

where α is a dimensionless exponent (≤ 1), providing information related to the number of traps (or defect states) present, and β is a parameter related to the photodetector responsivity [31]. α equals 1 in an ideal trap-free photodetector but becomes less than 1 in the presence of trap states. In our case, α is 0.46, showing that most traps are already filled at lower optical power densities. Additional illumination power raises the photocurrent less efficiently. The internal quantum efficiency (IQE), the ratio of the number of charge carriers or electron-hole pairs generated to the number of photons absorbed [32], is 50.12% for the same illumination conditions (with 97.73% absorption at 400 nm). There are a few possible reasons why a high absolute responsivity and high EQE (i.e., >100%) are measured. The higher external bias voltage above the barrier voltage leads to the generation of additional "non-light-driven" electron-hole pairs. At the illumination wavelength, which is much higher than the band gap of Te (0.34 eV [33] in homogeneous bulk tellurium but can be engineered up to approximately 1.42 eV by modulating its size at nanoscales [34]), more electron-hole pairs can be stimulated by avalanche multiplication per photon in the active region of the device. In addition, trapped minority carriers, electrons in our case, at the various defective states in our system, further enhance the internal gain. Although more than 100% EQE is not common, a high internal gain is possible by avalanche carrier multiplication [35], such as by metal-semiconductor-metal (*M-S-M*) photodetectors or *p-i-n* photodiodes [36].

The temporal evolution of the Te/TeO_2-glass nanocomposite is displayed in Fig. 3(e). The rise time, the time required for current to increase from 10% to 90% of its peak value under illumination, is one of the key parameters to evaluate a photodetector performance. We measured an average rise time of about 20 s, which is rather low. The carrier mobility of Te typically ranges from 20 to 50 cm^2/Vs at room temperature [37]. The mobility is also affected by the contribution of carriers present near the Te/TeO_2 interface [30]. Therefore, the delay in the rise time of the Te/TeO_2-glass interface is attributed to several factors, such as the existence of charge impurities, defects, or trap states. A decrease in the mobility of carriers can also be due to surface texture originating from the laser-induced self-organized nanostructures [1]. In addition, high photoconductive gain results in an excessive number of carriers (generally referred to as photomultiplication [38]), which is a slow process because the photocurrent generation rate is higher than the recombination rate in our case during the rise time. In contrast, the decay time, which is the time required for the current to decrease from 90% to 10% of its peak value, is an order of magnitude slower. Likewise, a slow photoconductive decay response can be attributed to a large number of recombination centers, the presence of many trap levels, and defect states within the band gap as such that recombination of minority carriers takes a longer time [39]. Relaxation curves are best fitted with a sum of two exponential functions, expressed as

$$I_{\text{ph}}(t) = I_{\text{dark}} + A_1 e^{-(t/\tau_1)} + A_2 e^{-(t/\tau_2)},$$

where A_1 and A_2 are weight coefficients, and τ_1 and τ_2 are the characteristic decay constants (effective relaxation times) [40,41]. While the average rise time is approximately 20 s, the decay time is about an order of magnitude longer [42]. This persistent photoconductivity is also observed in amorphous, metal-oxide semiconductors and wide-band-gap semiconductors [43,44]. Various reasons for the persistent photoconductivity are the presence of oxygen vacancies located within the band gap [43], large spatial fluctuations of the potential energy of charge carriers [44], point defects, and metastable defects [45]. In some cases, the persistent behavior can take a few hours to days without illumination. This behavior can be eliminated by designing a device with a three-gated terminal in a sandwich configuration, such as a field-effect transistor device structure, and subsequently by applying a short-pulse positive gate voltage [43,46]. For different wavelengths, Fig. S5 (see Supplemental Material [13]) shows the spectro-temporal evolution of the line patterns. The rise time is 82 s for white light, 55 s for 463 nm, and 41 s for 263 nm. The decay times for white light, 463 and 263 nm under the same illumination conditions are 411, 207, and 286 s, respectively. Various Te-based photodetector (whether macro- or nanoscale, from ultraviolet to near

TABLE I. Comparison of spectral range, responsivity, detectivity, the rise and decay time, and the stability of Te nanostructures and common photoconductive materials.

Sample	Spectral range (nm)	Responsivity at RT (A/W)	Detectivity (Jones)	The rise and decay times	Stability
This work	263, 400, 463 nm and white light	16.54 at 400 nm and 0.07 mW/cm^2	5.25×10^{11} at 400 nm	20 and 236 s	Cycling more than 2 months
Te nanowires [50]	633 nm	...	...	40 and 40 s	Cycling for 100 times
2D Te nanoplates [51]	413–550 nm	389.5 at 473 nm and 76.2 mW/cm^2	...	4.4 and 2.8 s	Bending for 100 times
2D Te nanoflakes [29]	1550 nm	51.85 at 1550 nm and 0.51 mW/mm^2	1.88×10^{10}	19 and 21 μs	...
2D Te nanoflakes [52]	520, 1550 and 3390 nm	383 at 520 nm and 1.6 nW	...	...	...
2D Te nanoflakes [46]	1400–2400 nm	16 at 1700nm	2×10^9	Order of few seconds each	...
2D Te nanosheets [28]	350–400 nm	13.4×10^{-6} at 350 nm and 2.17 mW/cm^2	3.1×10^7	54.5 and 70.2 ms	Cycle stability for 10 000 s
Te nanoparticles in PMMA [30]	310–2200 nm	7.5×10^{-8} at 400 nm and 4.2 mW/cm^2	...	...	...
Te nanosheets and nanowires [53]	830, 1310, 1550, 2000 nm and blackbody	6650 at 1550 nm and 0.01 mW/mm^2	1.23×10^{12}	31.7 and 25.5 μs	+3 months
Te nanorods [54]	300–785 nm	6.1 at 0.94 mW/cm^2	1.2×10^{11}	tens of seconds	~30 days
CdS nanobelts [55]	490 nm	7.3×10^4 at 3 mW/cm^2	...	~20 μs	More than 73 h
CdS nanorod [56]	365, 420, 450, 500 nm	1.23×10^4 at 450 nm and 0.5 mW/cm^2	2.8×10^{11}	0.82 and 0.84 s	...
CdSe nanocrystals [57]	500–532 nm	9.72 at 532 nm and 0.9 W/cm^2	6.9×10^{10}	both below 2 μs	...
t-Se nanoparticles [58]	300–700 nm	19×10^{-3} at 610 nm and 0.4 mW/cm^2	...	0.32 and 0.23 μs	...
ZnO nanowires [59]	350–500 nm	1109 at 356 nm	...	both ~ tens of seconds	...

infrared) shows the rise and decay times in the range of microseconds to a few hours [4,8,27–30].

While the response time is rather slow with these specimens, there are a few strategies that can be considered to reduce it. The first one is related to the geometry of the device. Decreasing the length, which is inversely proportional to the time [47], or considering various types of design symmetric or asymmetric designs [48] are two possible strategies among others. The second one is at the material level. Reducing grain boundaries by increasing the crystal size or achieving a single crystal, either by further exploring the laser parameters' landscape or postprocessing, such as thermal treatment, will reduce the response time. Furthermore, the glass composition could be further engineered. One could also consider adding metal nanoparticles to adjust the Fermi level in the band gap and decrease the resistance as shown previously [49].

Table I summarizes the performance of various Te nanostructures and other nanostructures of photoconductive semiconductors such as CdS, CdSe, *t*-Se, and ZnO. While the size of the other Te devices is nano- and microscale, the laser-written patterns range from a few millimeters to a centimeter in length and hundreds of nanometers to a few micrometers in thickness. The responsivity and the detectivity vary with the optical power density. While this device exhibits comparable responsivity and detectivity with devices based on other manufacturing principles, there is still room to improve the time response. Let us investigate the stability of the device over time, an essential point of practical applications.

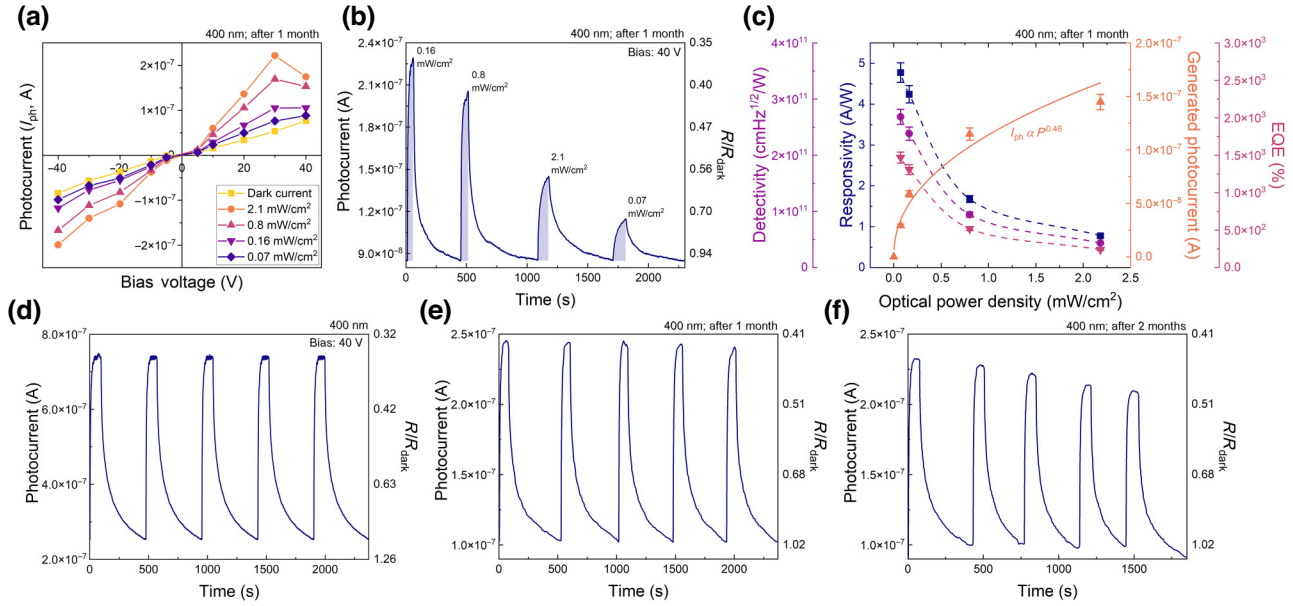

FIG. 4. (a) *I-V* curve without and with illumination at 400 nm for various voltage biases. The measurement was carried out a month after the fabrication of the device presented in Fig. 3. (b) Typical temporal evolution of photocurrent with different optical power densities (0.07–2.1 mW/cm^2) under 400-nm illumination 1 month after the fabrication of the device. (c) Responsivity, detectivity, EQE (%), and generated photocurrent of Te/TeO_2-glass nanocomposite structure 1 month after the fabrication of the device. (d)–(f) Repetitive temporal response at 400 nm with a flux of 2.1 mW/cm^2 observed on the day of the fabrication, after the first month and after the second month, respectively.

Figure 4 presents the photoconduction characteristics of the same device as in Fig. 3, from the day of fabrication to a few months after. Figure 4(a) shows *I-V* curves obtained without and with illumination at 400 nm after 1 month. We notice that the dark current decreases from 0.24 to 0.09 μA with a bias of +40 V after a month, and the current under illumination at 400 nm follows a similar trend. Figures 4(b) and 4(c) displays the temporal response upon various optical densities at 400 nm and corresponding responsivity, detectivity, quantum efficiency, and generated photocurrent values. R, D^*, and EQE (%) values degrade over a month under illumination at 400 nm, while the exponent of the generated photocurrent, α, stays the same. This behavior is attributed to trap states that are still present and that do not change over time. Finally, a repetitive measurement performed on the first day of the device fabrication is presented in Fig. 4(d), indicating the robustness and stability of the device. The amount of photoresponse and dark resistivity after 10 h of a cyclic test has not changed. Figures 4(e) and 4(f) show the multiple *on-off* cycles after a few months of usage. The rise and decay time does not change after a month except for the photocurrent value. However, after 2 months, there is a noticeable baseline drift of the generated photocurrent and response times. There are a few possibilities to explain this dramatic change in the photoresponse of the device over a few months. The first reason is the irreversible photoinduced oxidation upon UV illumination, observed previously in Te [4,7]. The oxidation of Te starts immediately after the first test of the device and forms TeO_2/Te/TeO_2-glass interface. However, the interface TeO_2/Te moves over time, as suggested by the dark-current value being less than the value on the first day. Further illumination causes the oxidation of Te nanocrystals and nanoparticles, which results in the dark current approaching zero. To understand the degradation mechanism under UV irradiation, Raman spectra of pristine glass and the laser-written line patterns were collected over time with a Raman laser emitting at 445 nm.

Raman spectra of the structural evolution of the tellurite glass under a Raman laser emitting at 445 nm are shown in Fig. 5(a). The glass network of the glass is composed of TeO_4 trigonal bipyramids (TBP), TeO_{3+1} distorted trigonal bipyramids (DTBP), TeO_3 trigonal pyramids (TP), WO_4, and WO_6 polyhedra. It results in the presence of Raman peaks, assigned to bending vibrations of W—O—W in WO_6 octahedra at 355 cm^{-1}, a symmetrical stretching of Te—O—Te linkages at 490 cm^{-1}, continuous network of TeO_4 at 610 cm^{-1}, antisymmetric stretching of Te—O—Te linkages consisting two inequivalent Te—O bonds at 670 cm^{-1}, Te and NBO of TeO_{3+1} and TeO_3 at 720 cm^{-1}, stretching of Te—O$^-$ in TeO_{3+1} and TeO_3 at 790 cm^{-1}, stretching of W—O, W—O$^-$ and W = O bonds associated with WO_4 and WO_6 polyhedra at 860 and 920 cm^{-1}, respectively [60,61]. There is no change in the peak intensity and ratio of the peaks in each spectrum collected at every 300 s. Hence, the

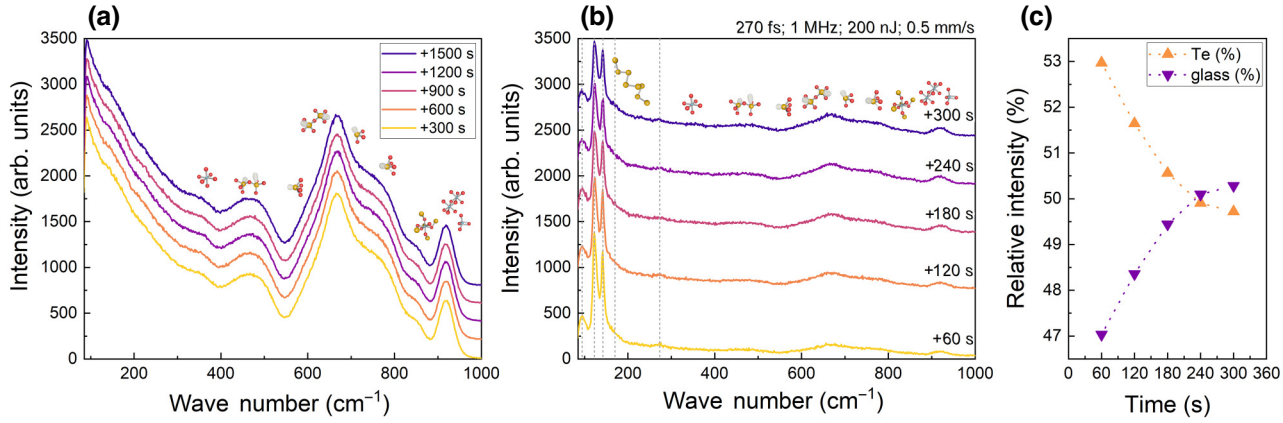

FIG. 5. (a) The Raman spectra of the pristine glass after irradiation with 445-nm-Raman laser for 1500 s. (b) The Raman spectra of the laser-irradiated line pattern after irradiation for 300 s. The femtosecond-laser processing parameters are 200 nJ with 0.5 mm/s at 1 MHz (corresponding to an incoming pulse fluence of 262 J/mm^2). Note that Raman investigation was performed on the same day as the fabrication of the tested sample. (c) The relative intensities of Te [$I_{93}+I_{122}+I_{141}+I_{170}+I_{260}$, (%)] and pristine glass peaks [$I_{356}+I_{470}+I_{610}+I_{670}+I_{720}+I_{790}+I_{860}+I_{920}$, (%)] at the laser-modified zone after being irradiated with Raman laser for 300 s. The optical power density of the Raman laser is 115 mW/μm^2.

glass substrate is not altered while characterizing the device.

Figures 5(b) and 5(c) displays the Raman spectra of the center of the laser-written pattern and the ratio of the Te versus TeO_2-glass. The characteristic vibration peaks of Te in the laser-modified zone located between 93 and 260 cm^{-1} correspond to E_1 (93), A_1 (118), and E_2 (139) modes, Te—Te homopolar bonds in amorphous Te (*a*-Te, 170 cm^{-1}), and second-order spectra (260) [7,62–64]. After irradiating for 300 s, the Raman spectra do not show any crystalline-TeO_2 peaks but rather a decrease in the intensity ratio of Te/TeO_2 glass and an increase in the intensity of the main glass bands. The photo-oxidation process further explains the longer decay time of the device after fabrication. Due to oxidation, the zones enriched with holes at the surface, the grain boundary, and the intragrain regions decrease. After 2 months of device usage, both rise and decay times decrease proportionally. Yet, time constants do not change, implying the presence of trap states as recombination centers. Fewer carriers are generating less photocurrent in each cycle, resulting in shorter recombination times. Transparent thin films of SiO_2 or Si_3N_4 can overcome the degradation of the patterns [25] by shielding the photoconductive layer from the environment. Another reason for the deterioration of the performances can be the degradation of the electrical contacts or the reaction between Te and the metal contacts (Au and Ag) [25]. Typical metal-contacted Te devices show a performance degradation over time and temperature (failure above 473 K) due to the diffusion of metal atoms into the Te channels. A nonreactive interlayer, such as graphene [25], can be employed to prevent metal diffusion. In summary, preventative steps against detrimental effects, such as the photo-oxidation of Te and the degradation of metallic contacts, are necessary for better stability of the photoconductivity properties.

IV. SUMMARY AND OUTLOOK

We observed a photoresponse of a tellurium and tellurite glass (Te/TeO_2-glass) nanocomposite interface produced by a femtosecond-laser direct-write process on a tellurite glass surface. After laser exposure, the measured resistivity is at least 10 orders of magnitude lower than the one of the unmodified material and is comparable to the one value measured for polycrystalline tellurium. By scanning a femtosecond laser beam over the tellurite glass substrate, one can write a conductive path between arbitrarily distant locations. Furthermore, we show that line patterns produced in this manner can have a highly reproducible and sensitive photoresponse, from the near ultraviolet to the visible spectrum, stable over a few months. This manufacturing process demonstrates that one can turn *a priori* nonphoto substrates with specific compositions, in the present case tellurite glass, into a photoconductive one by exposing it to a femtosecond laser *without adding any material to the substrate*.

SUPPORTING INFORMATION

Supporting information is available from the author.

ACKNOWLEDGMENTS

The Galatea Lab is thankful to the sponsorship of Richemont International and to Tokyo Institute of Technology (TIT) for providing the tellurite glass substrates. The authors are thankful to Samuel Benketaf for contributing to the PCB design, Adrien Toros for wire

bonding, and AQUA laboratory for providing a source measurement unit. The authors would like to thank Loïc Chautems for helping with the experimentation.

AUTHOR CONTRIBUTIONS

In this paper, G.T. wrote the draft paper and performed most of the experiments presented in this paper. G.T., A.R., and Y.B. designed and developed the mask and device fabrication process. G.T. and A.R. performed resistivity measurements over temperature and spectral and temporal response of as-produced samples. G.T., A.R., and Y.B. interpreted the experimental results and analyzed the experimental data. T.K. produced the bulk material and measurement data of various bulk properties. Y.B. supervised the research. All the authors discussed and revised the paper.

[1] G. Torun, T. Kishi, and Y. Bellouard, Direct-write laser-induced self-organization and metallization beyond the focal volume in tellurite glass, Phys. Rev. Mater. **5**, 055201 (2021).
[2] G. Torun, T. Kishi, D. Pugliese, D. Milanese, and Y. Bellouard, Formation mechanism of elemental Te produced in tellurite glass systems by femtosecond laser irradiation, Adv. Mater. **35**, 2210446 (2023).
[3] J. Sunada, K. Oishi, A. Kasai, and T. Kitahara, Photoconduction in Te thin film after exposure to UV light, Jpn. J. Appl. Phys. **21**, 1781 (1982).
[4] K. Oishi, K. Okamoto, and J. Sunada, Photoconduction on photo-oxidized tellurium thin films, Thin Solid Films **148**, 29 (1987).
[5] J. Sunada, K. Okamoto, K. Oishi, and S. Shimazu, UV photo-oxidation of Te films (photon energy dependence), Appl. Surf. Sci. **33–34**, 434 (1988).
[6] J. Sunada, Y. Hashimoto, K. Oishi, and K. ich Fukuchi, The role of oxygen species in photoconduction of surface oxidized Ge films, Phys. Lett. A **151**, 447 (1990).
[7] T. Vasileiadis and S. N. Yannopoulos, Photo-induced oxidation and amorphization of trigonal tellurium: A means to engineer hybrid nanostructures and explore glass structure under spatial confinement, J. Appl. Phys. **116**, 103510 (2014).
[8] J. Sunada, K. Osada, T. Namekawa, K. Oishi, and K. Fukuchi, Photoconduction in Te and Te-oxide bilayered film sensitive to UV light, Phys. Lett. A **146**, 85 (1990).
[9] M. Palomba, U. Coscia, G. Carotenuto, S. De Nicola, and G. Ambrosone, Fabrication and characterizations of films made of Te/TeO_2 nanopowder consolidated by poly(methyl methacrylate), Phys. Status Solidi C **12**, 1317 (2015).
[10] D. Tsiulyanu, S. Marian, V. Miron, and H. D. Liess, High sensitive tellurium based NO_2 gas sensor, Sens. Actuators, B **73**, 35 (2001).
[11] D. Tsiulyanu, Gas-sensing features of nanostructured tellurium thin films, Beilstein J. Nanotechnol. **11**, 1010 (2020).
[12] F. Arab, M. Mousavi-Kamazani, and M. Salavati-Niasari, Synthesis, characterization, and optical properties of Te, Te/TeO_2 and TeO_2 nanostructures: Via a one-pot hydrothermal method, RSC Adv. **6**, 71472 (2016).
[13] See the Supplemental Material at http://link.aps.org/supplemental/10.1103/PhysRevApplied.21.014008 for device preparation and additional results.
[14] R. N. Hampton, W. Hong, G. A. Saunders, and R. A. El-Mallawany, The electrical conductivity of pure and binary TeO_2 glasses, J. Non. Cryst. Solids **94**, 307 (1987).
[15] M. Çelikbilek, Ph.D. Thesis, Istanbul Technical University, 2013.
[16] R. W. McKay and W. E. Gravelle, The Hall effect and resistivity of tellurium, Can. J. Phys. **39**, 534 (1961).
[17] A. Nussbaum, Electrical properties of pure tellurium and tellurium-selenium alloys*, Phys. Rev. **94**, 337 (1954).
[18] M. A. Dinno, M. Schwartz, and B. Giammara, Structural dependence of electrical conductivity of thin tellurium films, J. Appl. Phys. **45**, 3328 (1974).
[19] G. Fischer, G. K. White, and S. B. Woods, Thermal and electrical resistivity of tellurium at low temperatures, Phys. Rev. **106**, 480 (1957).
[20] X. Zhang, J. Jiang, A. A. Suleiman, B. Jin, X. Hu, X. Zhou, and T. Zhai, Hydrogen-assisted growth of ultrathin Te flakes with giant gate-dependent photoresponse, Adv. Funct. Mater. **29**, 1906585 (2019).
[21] X. Zhao, J. Shi, Q. Yin, Z. Dong, Y. Zhang, L. Kang, Q. Yu, C. Chen, J. Li, X. Liu, *et al.*, Controllable synthesis of high-quality two-dimensional tellurium by a facile chemical vapor transport strategy, IScience **25**, 103594 (2022).
[22] C. Ma, J. Yan, Y. Huang, C. Wang, and G. Yang, The optical duality of tellurium nanoparticles for broadband solar energy harvesting and efficient photothermal conversion, Sci. Adv. **4**, eaas9894 (2018).
[23] P. Makuła, M. Pacia, and W. Macyk, How to correctly determine the band gap energy of modified semiconductor photocatalysts based on UV-Vis spectra, J. Phys. Chem. Lett. **9**, 6814 (2018).
[24] D. Tsiulyanu and O. Mocreac, Concentration induced damping of gas sensitivity in ultrathin tellurium films, Sens. Actuators, B **177**, 1128 (2013).
[25] C. Zhao, L. Hurtado, and A. Javey, Thermal stability for Te-based devices, Appl. Phys. Lett. **117**, 192104 (2020).
[26] V. Selamneni, T. Akshaya, V. Adepu, and P. Sahatiya, Laser-assisted micropyramid patterned PDMS encapsulation of 1D tellurium nanowires on cellulose paper for highly sensitive strain sensor and its photodetection studies, Nanotechnology **32**, 455201 (2021).
[27] M. Peng, *et al.*, Room-temperature blackbody-sensitive and fast infrared photodetectors based on 2D tellurium/graphene van der Waals heterojunction, ACS Photonics **9**, 1775 (2022).
[28] Z. Xie, C. Xing, W. Huang, T. Fan, Z. Li, J. Zhao, Y. Xiang, Z. Guo, J. Li, Z. Yang, *et al.*, Ultrathin 2D nonlayered tellurium nanosheets: Facile liquid-phase exfoliation, characterization, and photoresponse with high performance and enhanced stability, Adv. Funct. Mater. **28**, 1 (2018).
[29] Y. Yan, K. Xia, W. Gan, K. Yang, G. Li, X. Tang, L. Li, C. Zhang, G. T. Fei, and H. Li, A tellurium short-wave

infrared photodetector with fast response and high specific detectivity, Nanoscale **14**, 13187 (2022).
[30] U. Coscia, G. Ambrosone, M. Palomba, S. Binetti, A. Le Donne, D. Siliqi, and G. Carotenuto, Photoconductivity of tellurium-poly(methyl methacrylate) in the ultraviolet–visible-near infrared range, Appl. Surf. Sci. **457**, 229 (2018).
[31] Q. Zhao, W. Wang, F. Carrascoso-Plana, W. Jie, T. Wang, A. Castellanos-Gomez, and R. Frisenda, The role of traps in the photocurrent generation mechanism in thin InSe photodetectors, Mater. Horiz. **7**, 252 (2020).
[32] Q. Zhang, J. Jie, S. Diao, Z. Shao, Q. Zhang, L. Wang, W. Deng, W. Hu, H. Xia, X. Yuan, *et al.*, Solution-processed graphene quantum dot deep-UV photodetectors, ACS Nano **9**, 1561 (2015).
[33] H. G. Junginger, Electronic band structure of tellurium, Solid State Commun. **5**, 509 (1967).
[34] A. Kramer, M. L. Van de Put, C. L. Hinkle, and W. G. Vandenberghe, Tellurium as a successor of silicon for extremely scaled nanowires: A first-principles study, npj 2D Mater. Appl. **4**, 10 (2020).
[35] M. Razeghi and A. Rogalski, Semiconductor ultraviolet detectors, J. Appl. Phys. **79**, 7433 (1996).
[36] F. Alema, B. Hertog, O. Ledyaev, D. Volovik, R. Miller, A. Osinsky, S. Bakhshi, and W. V. Schoenfeld, High responsivity solar blind photodetector based on high Mg content MgZnO film grown via pulsed metal organic chemical vapor deposition, Sens. Actuators, A **249**, 263 (2016).
[37] K. Okuyama and Y. Kumagai, Hall mobility of evaporated tellurium films, Jpn. J. Appl. Phys. **12**, 1884 (1973).
[38] J. Miao and C. Wang, Avalanche photodetectors based on two-dimensional layered materials, Nano Res. **14**, 1878 (2021).
[39] P. Bhaskar, A. W. Achtstein, M. J. W. Vermeulen, and L. D. A. Siebbeles, Charge mobility and recombination mechanisms in tellurium van der Waals solid, J. Phys. Chem. C **123**, 841 (2019).
[40] V. D. Popovych and M. Bester, Measurements of Photoconductive transients in vapor grown CdTe : Cl over wide temperature and dopant concentration ranges, J. Appl. Phys. **112**, 023705 (2012).
[41] D. Guo, Y. Su, H. Shi, P. Li, N. Zhao, J. Ye, S. Wang, A. Liu, Z. Chen, C. Li, *et al.*, Self-powered ultraviolet photodetector with superhigh photoresponsivity (3.05 A/W) based on the GaN/Sn:Ga_2O_3 Pn junction, ACS Nano **12**, 12827 (2018).
[42] Y. Zhang, D. J. Hellebusch, N. D. Bronstein, C. Ko, D. F. Ogletree, M. Salmeron, and A. P. Alivisatos, Ultrasensitive photodetectors exploiting electrostatic trapping and percolation transport, Nat. Commun. **7**, 11924 (2016).
[43] S. Jeon, S.-E. Ahn, I. Song, C. Jung Kim, U.-I. Chung, E. Lee, I. Yoo, A. Nathan, S. Lee, K. Ghaffarzadeh, *et al.*, Gated three-terminal device architecture to eliminate persistent photoconductivity in oxide semiconductor photosensor arrays, Nat. Mater. **11**, 301 (2012).
[44] A. George, M. V. Fistul, M. Gruenewald, D. Kaiser, T. Lehnert, R. Mupparapu, C. Neumann, U. Hübner, M. Schaal, N. Masurkar, *et al.*, Giant persistent photoconductivity in monolayer MoS_2 field-effect transistors, npj 2D Mater. Appl. **5**, 15 (2021).
[45] E. Arslan, S. Bütün, S. B. Lisesivdin, M. Kasap, S. Ozcelik, and E. Ozbay, The persistent photoconductivity effect in AlGaN/GaN heterostructures grown on sapphire and SiC substrates, J. Appl. Phys. **103**, 103701 (2008).
[46] M. Amani, C. Tan, G. Zhang, C. Zhao, J. Bullock, X. Song, H. Kim, V. R. Shrestha, Y. Gao, K. B. Crozier, *et al.*, Solution-synthesized high-mobility tellurium nanoflakes for short-wave infrared photodetectors, ACS Nano **12**, 7253 (2018).
[47] L. Chen, P. Dong, and M. Lipson, High performance germanium photodetectors integrated on submicron silicon waveguides by low temperature wafer bonding, Opt. Express **16**, 11513 (2008).
[48] C. Wu, F. Wu, H. Hu, C. Ma, J. Ye, S. Wang, H. Wu, J. Wang, A. Liu, and D. Guo, Work function tunable laser induced graphene electrodes for Schottky type solar-blind photodetectors, Appl. Phys. Lett. **120**, 101102 (2022).
[49] K. Liu, M. Sakurai, M. Liao, and M. Aono, Giant improvement of the performance of ZnO nanowire photodetectors by Au nanoparticles, J. Phys. Chem. C **114**, 19835 (2010).
[50] Y. Wang, Z. Tang, P. Podsiadlo, Y. Elkasabi, J. Lahann, and N. A. Kotov, Mirror-like photoconductive layer-by-layer thin films of Te nanowires: The fusion of semiconductor, metal, and insulator properties, Adv. Mater. **18**, 518 (2006).
[51] Q. Wang, M. Safdar, K. Xu, M. Mirza, Z. Wang, and J. He, van der Waals epitaxy and photoresponse of hexagonal tellurium nanoplates on flexible mica sheets, ACS Nano **8**, 7497 (2014).
[52] C. Shen, *et al.*, Tellurene photodetector with high gain and wide bandwidth, ACS Nano **14**, 303 (2020).
[53] M. Peng, *et al.*, Blackbody-sensitive room-temperature infrared photodetectors based on low-dimensional tellurium grown by chemical vapor deposition, Sci. Adv. **7**, abf7358 (2021).
[54] Q. Xiao, X. Li, Z. Zhang, C. Hu, G. Dun, B. Sun, Y. Peng, Q. Wang, Z. Zheng, and H. Zhang, Facile fabrication of highly uniform tellurium nanorods for self-powered flexible optoelectronics, Adv. Electron. Mater. **6**, 2000240 (2020).
[55] L. Li, P. C. Wu, X. S. Fang, T. Y. Zhai, L. Dai, M. Y. Liao, Y. Koide, H. Q. Wang, Y. Bando, and D. Golberg, Single-crystalline CdS nanobelts for excellent field-emitters and ultrahigh quantum-efficiency photodetectors, Adv. Mater. **22**, 3161 (2010).
[56] W. Zhao, L. Liu, M. Xu, X. Wang, T. Zhang, Y. Wang, Z. Zhang, S. Qin, and Z. Liu, Single CdS nanorod for high responsivity UV–visible photodetector, Adv. Opt. Mater. **5**, 1700159 (2017).
[57] W. Xing, S.-C. Kung, W. E. van der Veer, W. Yan, T. Ayvazian, J. Y. Kim, and R. M. Penner, High-throughput fabrication of photoconductors with high detectivity, photosensitivity, and bandwidth, ACS Nano **6**, 5627 (2012).
[58] K. Hu, H. Chen, M. Jiang, F. Teng, L. Zheng, and X. Fang, Broadband photoresponse enhancement of a high-performance t-Se microtube photodetector by plasmonic metallic nanoparticles, Adv. Funct. Mater. **26**, 6641 (2016).
[59] K. Keramatnejad, F. Khorramshahi, S. Khatami, and E. Asl-Soleimani, Optimizing UV detection properties of N-ZnO nanowire/p-Si heterojunction photodetectors by using a porous substrate, Opt. Quantum Electron. **47**, 1739 (2015).

[60] T. Kosuge, Y. Benino, V. Dimitrov, R. Sato, and T. Komatsu, Thermal stability and heat capacity changes at the glass transition in K_2O–WO_3–TeO_2 glasses, J. Non-Cryst. Solids **242**, 154 (1998).

[61] M. Çelikbilek Ersundu, A. E. Ersundu, M. I. Sayyed, G. Lakshminarayana, and S. Aydin, Evaluation of physical, structural properties and shielding parameters for K_2O–WO_3–TeO_2 glasses for gamma ray shielding applications, J. Alloys Compd. **714**, 278 (2017).

[62] C. Marini, D. Chermisi, M. Lavagnini, D. Di Castro, C. Petrillo, L. Degiorgi, S. Scandolo, and P. Postorino, High-pressure phases of crystalline tellurium: A combined Raman and ab initio study, Phys. Rev. B **86**, 064103 (2012).

[63] Y. H. Cheng, S. W. Teitelbaum, F. Y. Gao, and K. A. Nelson, Femtosecond laser amorphization of tellurium, Phys. Rev. B **98**, 134112 (2018).

[64] R. T. Ananth Kumar, H. A. Mousa, P. Chithra Lekha, S. T. Mahmoud, and N. Qamhieh, Scrutiny of structural disorder using Raman spectra and Tauc parameter in $GeTe_2$ thin films, J. Phys.: Conf. Ser. **869**, 012018 (2017).